

Refractive elastic scattering of carbon and oxygen nuclei: The mean field analysis and Airy structures

S. Szilner^{a,b}, M.P. Nicoli^b, Z. Basrak^a, R.M. Freeman^b, F. Haas^b, A. Morsad^c, M. E. Brandan^d, and G. R. Satchler^e

^a*Ruđer Bošković Institute, HR-10 002 Zagreb, Croatia*

^b*Institut de Recherches Subatomiques, CNRS-IN2P3/ULP, Strasbourg, France*

^c*Faculté des Sciences Ben M'Sik, Université Hassan II, Casablanca, Morocco*

^d*Instituto de Física, UNAM, Mexico, Mexico*

^e*University of Tennessee, Knoxville and Oak Ridge National Laboratory, USA*

The experimental data on the $^{16}\text{O}+^{12}\text{C}$ and $^{18}\text{O}+^{12}\text{C}$ elastic scatterings and their optical model analysis are presented. Detailed and complete elastic angular distributions have been measured at the Strasbourg Vivitron accelerator at several energies covering the energy range between 5 and 10 MeV per nucleon. The elastic scattering angular distributions show the usual diffraction pattern and also, at larger angles, refractive effects in the form of nuclear rainbow and associated Airy structures. The optical model analysis unambiguously shows the evolution of the refractive scattering pattern. The observed structure, namely the Airy minima, can be consistently described by a nucleus-nucleus potential with a deep real part and a weakly absorptive imaginary part. The difference in absorption in the two systems is explained by an increased imaginary (mostly surface) part of the potential in the $^{18}\text{O}+^{12}\text{C}$ system. The relation between the obtained potentials and those reported for the symmetrical $^{16}\text{O}+^{16}\text{O}$ and $^{12}\text{C}+^{12}\text{C}$ systems is drawn.

PACS numbers: 25.70.Bc, 25.70.-z, 24.10.Ht

I. INTRODUCTION

Significant progress has been made in the last decade in the understanding and determination of the nuclear optical potential for light heavy-ion systems. In the description of heavy-ion collisions and the accompanying compound nucleus formation, the strongly absorptive interaction is usually present. In certain light heavy-ion collisions, involving closed or semiclosed shell nuclei, the number of open reaction channels is small and the absorption is weaker [1]. Consequently, resonant and refractive phenomena have been observed in these systems. Recent reviews of theoretical and experimental results on resonant and refractive phenomena can be found in [2–4]. Reported systematic measurements of the elastic scattering which cover broad angular and energy ranges and their optical model analysis have resulted in a deeper insight into the dynamics of light heavy-ion scattering. Such progress is closely connected with the observation of refractive effects. It has been shown that the presence of the nuclear rainbow and, the associated Airy structure in elastic scattering reduces the ambiguities of the optical potential character (shallow or deep). The existence of systematic studies, where the change of potential parameters can be followed as a function of energy, is essential for the determination of a unique nucleus-nucleus potential at different energies and in different systems.

The main features of the optical rainbow lie in the refraction and reflection. In the case of interference due to the contributions around the maximum deflection angle, higher-order maxima, i.e., Airy structure, appear inside the lighted region. The observation of the rainbow pattern in heavy-ion collisions is closely connected with the degree of transparency. Water is transparent to visible light, while the nuclear rainbow is damped by the presence of absorption. The rainbow scattering appears when the nuclear potential is strong enough to deflect particles into negative angles (so-called farside). The combination of these two features, deep real potential and incomplete absorption, makes possible the observation of distinct refractive effects like the Airy minima, the rainbow angle and, the rainbow dark side.

The energy range between 5 and 10 MeV per nucleon can be defined as an intermediate region lying between that where the molecular-resonant states show up and that with the prominent appearance of the nuclear rainbow. The experimental results on binary channels reported up to very recently in the literature for this energy range are rather scarce. The refractive studies have mainly involved symmetrical systems, mostly $^{12}\text{C}+^{12}\text{C}$ [5–7] and $^{16}\text{O}+^{16}\text{O}$ [8–10]. To cover the lack of systematic measurements, several experiments have been performed at the Strasbourg Vivitron accelerator, which is well suited for studies in this intermediate energy range. Detailed and complete elastic angular distributions have

been measured for three systems: $^{16}\text{O}+^{16}\text{O}$, $^{16}\text{O}+^{12}\text{C}$, and $^{18}\text{O}+^{12}\text{C}$. In this work we concentrate on the study of the nonidentical systems where the angles beyond 90° can be explored directly.

In the literature, the data for the $^{16}\text{O}+^{12}\text{C}$ system are not as complete and numerous as for identical boson systems. Relative to the ^{16}O beam energies of the present work, the elastic scattering angular distributions have been reported and analyzed at higher energies: $E_{\text{lab}} = 132$ [11], 139, 216, and 311 MeV [12], 608 [13], and 1503 MeV [14], and at lower energies: $E_{\text{lab}} = 24, 35, 45$ [15], 65, and 80 [16,17] MeV. The data reported in Refs. [12,15,16] cover only limited angular ranges and do not reveal any significant refractive features. The data at 608 and 1503 MeV have been shown to contain some refractive effects displaying sensitivity to the features of the real potential. Recently, the elastic scattering measurements over a wide angular range have been published at energies just above the energy range covered in our study, i.e. at $E_{\text{lab}}=132$ (re-measured and extended to large angles), 170, 200, and 230 MeV [18]. No refractive study of the $^{18}\text{O}+^{12}\text{C}$ system has been reported in the literature so far.

Our elastic scattering data and the optical model analysis for the $^{16}\text{O}+^{16}\text{O}$ symmetric system were presented in [19–21], and for the $^{16}\text{O}+^{12}\text{C}$ system in [22]. The preliminary results on the $^{18}\text{O}+^{12}\text{C}$ scattering we presented in [23,24]. In this article, we report on an additional optical potential analysis of the $^{16}\text{O}+^{12}\text{C}$ and $^{18}\text{O}+^{12}\text{C}$ systems. In particular, we present the nearside-farside decomposition of the deduced potentials which allowed one to identify Airy minima and to follow their evolution as a function of beam energy. To have a better connection with the higher-energy domain, in the analysis of the $^{16}\text{O}+^{12}\text{C}$ system we have included the lowest energy (132 MeV) elastic scattering angular distribution reported in [18]. The change of the potential due to the addition of two extra neutrons in the $^{18}\text{O}+^{12}\text{C}$ system will be explicitly discussed.

II. EXPERIMENTS

The three reactions $^{16}\text{O}+^{12}\text{C}$, $^{18}\text{O}+^{12}\text{C}$, and $^{16}\text{O}+^{16}\text{O}$ were studied under the same experimental condition, which will be briefly described in this section. More details can be found in Refs. [25,26].

The elastic scattering angular distributions were measured at laboratory angles between 5° and 20° in steps of 0.5 degree using the Q3D magnetic spectrometer and its associated detection system. At larger angles all binary channels were recorded simultaneously using a fixed kinematical-coincidence setup composed of two position-sensitive (PS) silicon detectors. The setup allowed complete mass and Q -value identification of the binary fragments. PS detectors were placed on both sides of the beam ($15^\circ \leq \theta \leq 50^\circ$ and $-35^\circ \leq \theta \leq$

-70°) at 7.8 cm from the target, a self-supporting carbon film $\sim 20\mu\text{g}/\text{cm}^2$ thick. The $^{16}\text{O}+^{12}\text{C}$ and $^{18}\text{O}+^{12}\text{C}$ elastic scatterings were measured at beam energies $E_{\text{lab}}(^{16}\text{O})=62, 75, 80, 94.8, 100, 115.9,$ and 124 MeV and, at $E_{\text{lab}}(^{18}\text{O})=66.2, 85, 100,$ and 120 MeV, respectively. The electronics and data acquisition system of the Q3D spectrometer with the proportional counter in its focal plane and of the PS detectors in the kinematical-coincidence mode were independent of each other. The two detection systems had an overlapping angular region. The obtained center-of-mass elastic scattering angular distributions span the angular range between 10° and more than 140° for both systems studied with good statistics at all measured energies.

All angular distributions and the optical model description of the $^{16}\text{O}+^{12}\text{C}$ system were reported in [22]. In the present work we intend to study in more detail the connection with the higher-energy region. Thus, we are not going to discuss the results obtained at the two lowest energies, 62 and 75 MeV. In fact, it has recently been shown that at even lower energies the deep real potential describes both the observed structure in the fusion excitation function and the gross features of elastic angular distributions [17].

Resonant phenomena in heavy-ion reactions are usually restricted to systems composed of the so-called α -particle nuclei. Considering the presence of resonances as a signature of weak absorption, one would expect the refractive effects to appear in the higher-energy domain for the same systems. A description of all details that appear in angular distributions where the resonant effects are superimposed on the gross structure is unlikely to be achieved with a mean field approach, i.e., the optical model. This is the case with the $^{18}\text{O}+^{12}\text{C}$ system at $E_{\text{lab}}=66.12$ MeV, the lowest energy of the present measurement. At this energy a broad resonance has been reported and the energy spectra and angular distributions of the binary channels were discussed in [25,27].

III. OPTICAL MODEL POTENTIAL

In the analysis of the $^{16}\text{O}+^{16}\text{O}$ [19–21] and $^{16}\text{O}+^{12}\text{C}$ [22] systems several choices were tried for the real part of the potential. Our understanding of the properties and microscopic grounds of the optical potential is largely based upon the folding model using a realistic nucleon-nucleon effective interaction [28]. The energy- and density-dependent interaction was used to generate a microscopic potential, which together with a phenomenological imaginary term, successfully describes our $^{16}\text{O}+^{16}\text{O}$ and $^{16}\text{O}+^{12}\text{C}$ data as well as the collisions in slightly higher and lower energy domains [9,17]. The resulting folded potentials are strongly attractive, and weakly energy dependent. It has been shown (see Fig. 1 in [22]) that the square of the Woods-Saxon form factor (WS2) with a suitable choice of radius and diffuseness

gives a shape that is very close to the folded potential. Indeed, equivalent fits to the data are found with either the folded or the WS2 potentials. In the present case, the real part of the potential is taken in the WS2 form:

$$V(r) = -V[f_V(r)]^2, \quad (1)$$

$$f_V = [1 + \exp(\frac{r - R_V}{a_V})]^{-1}.$$

The shape of the folded potential for the $^{16}\text{O}+^{12}\text{C}$ system is closely reproduced by Eq. (1) with the radius $R_V = 4.0$ fm and the surface diffuseness $a_V = 1.4$ fm. These values were kept constant throughout the best-fit automatic parameter searching procedure. In the energy range considered, no significant improvement of the fit was obtained by allowing R_V and a_V to vary freely. Slightly different values of the radius and diffuseness of the real potential for $^{18}\text{O}+^{12}\text{C}$ were adopted owing to the addition of the two neutrons. They were kept constant throughout the fitting procedures at the values $R_V = 4.08$ fm and $a_V = 1.38$ fm.

Two choices were used for the imaginary potential, a pure "volume" term of the Woods-Saxon (WS) type (W_{WS}) and a volume term together with an additional "surface" term ($W_{\text{WS2}} + W_{\text{D}}$). For the second choice of the imaginary potential we adopted the WS2 form factor for the volume term, and the radial derivate of the WS form for the additional surface term. The imaginary potentials are thus given by the following equations:

$$W(r) = W_{\text{WS}}(r) = -iW[f_W(r)], \quad (2)$$

$$\begin{aligned} W(r) &= W_{\text{WS2}}(r) + W_{\text{D}}(r) \\ &= -iW[f_W(r)]^2 - iW_{\text{D}}f_{\text{D}}(r), \end{aligned} \quad (3)$$

$$f_W = [1 + \exp(\frac{r - R_W}{a_W})]^{-1},$$

$$f_{\text{D}}(r) = -4a_{\text{D}} \frac{d}{dr} [1 + \exp(\frac{r - R_{\text{D}}}{a_{\text{D}}})]^{-1}.$$

In the following text, the optical potentials defined by Eqs. (1) and (2) will be called parameterization $P(W_{\text{WS}})$ and those defined by Eqs. (1) and (3) will be called parameterization $P(W_{\text{WS2}} + W_{\text{D}})$. The fits were obtained through the automatic search option in the program PTOLEMY [29].

The usual χ^2 criterion was used to judge the quality of agreement with the data:

$$\chi^2 = \frac{1}{N_{\sigma} - N_{\text{P}}} \sum_{i=1}^{N_{\sigma}} \frac{(\sigma_{\text{th}}^i - \sigma_{\text{ex}}^i)^2}{(\Delta\sigma_{\text{ex}}^i)^2}. \quad (4)$$

The σ_{th} and σ_{ex} are theoretical and experimental cross sections, $\Delta\sigma_{\text{ex}}$ are the uncertainties in the experimental cross sections, N_{σ} is the total number of angles at which

measurements were carried out, and N_{P} is the number of free fitting parameters. Two choices for the cross section uncertainties were considered. We either used the experimental cross section uncertainties or a fixed percentage of the experimental cross section for all measured angles. Compared with forward angles, the experimental cross-section uncertainties can be relatively large at intermediate and backward angles owing to the smaller cross section. Thus, the searching procedure does not give sufficient weight to those angles at which the refractive effects are expected to be observed. We have found that using a uniform percentage (10%) a better fit at intermediate and backward angles can be obtained.

For an interaction potential $U_{\text{E}}(r)$ between nuclei with nucleon numbers A_1 and A_2 , the volume integral

$$J_{\text{U}}(E) = -\frac{4\pi}{A_1 A_2} \int U_{\text{E}}(r)r^2 dr \quad (5)$$

is a sensitive measure of the potential strength. This definition applies to the real and imaginary parts of $U_{\text{E}}(r)$. Generally, the optical model analyses can give several discrete families of real potentials that fit an angular distribution equally well. It has been shown that the volume integrals are valuable tools for classifying different optical model families, especially in terms of global systematics, when different systems are compared.

The simple optical model potential is a local, angular-momentum independent potential. Thus, effects like the elastic transfer, an α -transfer in $^{16}\text{O}+^{12}\text{C}$ or a ^6He -transfer in $^{18}\text{O}+^{12}\text{C}$, which can introduce additional structure in the angular distribution, are not included.

The obtained angular distributions are complicated to interpret owing to the contributions and interferences of many involved partial waves. For this purpose, the nearside-farside decomposition technique, first presented by Fuller [30], is a helpful method for interpreting the optical model results. The nearside-farside decomposition separates the trajectories which originate from two different sides of the scattering potential. By convention, the nearside and farside correspond to classical trajectories with positive and negative deflection angles, respectively. The interference between nearside and farside trajectories will lead to the Fraunhofer diffraction pattern, and the interference between two farside components (the one more peripheral and the other more in the interior) will lead to the rainbow pattern. The refractive effects, namely the Airy minima and maxima, will therefore be present in the farside component. The crucial condition for the observation of refractive effects is incomplete absorption. The absorption should be weak enough ("transparency") to allow the inner farside component to be effective. The appearance of Airy oscillations in an angular distribution is a direct indication of interferences between waves which are bent by the nuclear mean field and provides a unique information on the potential at small interaction radii.

IV. ELASTIC ANGULAR DISTRIBUTIONS

A. Optical model description

Figures 1 and 2 show the data and the phenomenological model fits (thick-solid curves) of the angular distributions for the $^{16}\text{O}+^{12}\text{C}$ and $^{18}\text{O}+^{12}\text{C}$ systems, respectively. The parameters obtained using the fitting procedure are listed in Table I (parameters $P(W_{\text{WS2}} + W_{\text{D}})$ which are used on the left panels of both figures) and Table II ($P(W_{\text{WS}})$ and the right panels of Figs. 1 and 2).

The main features of the measured angular distributions, namely, the forward fine Fraunhofer diffractive oscillations and the broad structure at larger angles are well described by the calculation. An increase in cross sections at large angles is predicted by the calculations, but is smaller in some cases than observed experimentally.

In our previous analyses of the $^{16}\text{O}+^{16}\text{O}$ system [21], it was shown that for the data at the three highest energies (124, 115.9, and 103.1 MeV) an acceptable description was possible using just a volume term for the imaginary part. The fits at lower energies (lower than 100 MeV) required inclusion of a surface imaginary term. To be consistent, in the present analyses, the $^{16}\text{O}+^{16}\text{O}$ data at all energies were analyzed using both imaginary terms, volume and surface. The resulting imaginary potential is mostly of the volume type at higher energies. At lower energies the imaginary potential has a sharp-edged volume term and a surface term which peaks outside the volume one (see the top-right panel of Fig. 9). The initial set of parameters for the fits of the $^{16}\text{O}+^{12}\text{C}$ system was the one which gives the same volume integrals of the real and imaginary parts (Eq. 5) as those obtained in the fitting procedure for the $^{16}\text{O}+^{16}\text{O}$ system. The final difference between the volume integrals of the $^{16}\text{O}+^{16}\text{O}$ and $^{16}\text{O}+^{12}\text{C}$ systems at 124 MeV is $\sim 10\%$. In the optical model analysis of the $^{16}\text{O}+^{12}\text{C}$ system presented in [22], at all measured energies the folding and WS2 terms were used for the real potential and the sum of the volume (WS) and surface terms for the imaginary potential. It has to be noted that the imaginary volume term in [22] was of the WS type, while in the present analysis it is of the WS2 type when the surface term is included, which results in slightly different parameters. The main goal of this work is to establish a connection with the higher-energy domain and to identify the Airy minima and their order using the nearside-farside decomposition technique. To fulfill this task, we included in our study the angular distribution at 132 MeV [18]. The optical model analysis presented in [18] was performed by using for the real part either the folding or the phenomenological Woods-Saxon potentials. For the imaginary part, only a volume term was used (WS at all energies and WS2 at several energies). Such a potential, with only a volume imaginary term, describes the main features of the measured distributions, but fails to describe the backward-angle oscilla-

tions which become more important as energy decreases. Such a potential underestimates the observed increase of the yield at backward angles.

Actually, a satisfactory description of the whole structure observed in the $^{16}\text{O}+^{12}\text{C}$ system in the energy range considered, required the inclusion of an imaginary surface term. To justify this statement, the analysis with and without the imaginary surface term is consistently carried out and presented. Indeed, the distributions calculated without the surface term resulted in too little structure at large angles (Figs. 1 and 2, right panels). In addition, the predicted increase of yield at backward angles (in agreement with data) is less pronounced when the cross section is calculated using the imaginary volume term only. It seems that for a certain energy range, the data cannot be sufficiently well described without the surface term and that the $^{16}\text{O}+^{12}\text{C}$ and $^{18}\text{O}+^{12}\text{C}$ systems at the energies considered here are within this range.

For the $^{18}\text{O}+^{12}\text{C}$ system, the fits were obtained starting from the parameters of the $^{16}\text{O}+^{12}\text{C}$ system. The results of this procedure at an energy of 100 MeV, can be seen in Fig. 3. The top panel shows the best fit of the $^{16}\text{O}+^{12}\text{C}$ system with two different sets of parameters, using the sum of the volume and surface terms (solid curve) and using the volume term only (dashed curve). These sets of optical potential parameters were used to calculate the angular dependence for the $^{18}\text{O}+^{12}\text{C}$ system. The results of the calculation are superimposed on the $^{18}\text{O}+^{12}\text{C}$ data in the middle panel of Fig. 3. Agreement between measured and calculated values is reasonable at forward angles, but the calculated angular distributions cannot describe the two orders of magnitude smaller yield in the $^{18}\text{O}+^{12}\text{C}$ system at larger angles. It is worth noting that even without fitting, the number of oscillations in the calculation obtained using the imaginary term composed of the volume and surface terms (solid curve) agrees with the measurement throughout the angular range and over eight orders of magnitude of the differential cross section. The bottom panel of Fig. 3 shows the results of the fitting procedure. The differences between the potentials of the two systems are presented in Fig. 4: The left-bottom panel refers to the $P(W_{\text{WS}})$ parametrization and the right-bottom panel to the $P(W_{\text{WS2}} + W_{\text{D}})$ one. The real part remains almost unchanged, but the imaginary volume integral increases substantially from $^{16}\text{O}+^{12}\text{C}$ to $^{18}\text{O}+^{12}\text{C}$. To describe the decrease of the yield at backward angles, the absorption has to be increased. In the imaginary part of the potential which is composed of the volume and surface terms, the surface term now becomes dominant at large interaction radii.

The obtained potentials have deep real parts. When the additional surface term in the imaginary potential is included, the volume term has a smaller radius than the surface term and as a consequence, the volume imaginary potential has an almost square profile whose detailed shape depends on the system and energy.

The volume diffuseness of the imaginary potential tends to be very small when the surface imaginary term is included in the potential. The volume imaginary diffuseness could be fixed at some small values, such as 0.1 fm, without any significant change of the fits, but we rather report the values resulting from the automatic search.

The importance of the volume integrals can be shown by comparing the results of the two different parameterizations, $P(W_{\text{WS}})$ and $P(W_{\text{WS2}} + W_{\text{D}})$. The potentials which belong to $P(W_{\text{WS}})$ and $P(W_{\text{WS2}} + W_{\text{D}})$ at 100 MeV are shown in Fig. 4: left-top panel for the $^{16}\text{O}+^{12}\text{C}$ and right-top panel for the $^{18}\text{O}+^{12}\text{C}$ systems, respectively. The dashed curves correspond to $P(W_{\text{WS}})$, while the solid curves correspond to the $P(W_{\text{WS2}} + W_{\text{D}})$. The two solutions give the same (within a few percent) volume integrals (see Table III). In the imaginary part, when the individual surface and volume terms are considered, both terms are important. As mentioned above, the common characteristic of the $W_{\text{WS2}} + W_{\text{D}}$ solutions is that the volume imaginary term tends to have a sharp edge and a smaller radius than the surface term. The precise balance between the two imaginary terms is not so well established as the values of the integrals. The imaginary potential consisting of the volume term only, tends to smooth out the potential pocket of the $P(W_{\text{WS2}} + W_{\text{D}})$ in a way as to keep the imaginary volume integral about the same.

The volume integrals of the real potentials are very similar for both parameterizations and also for the phenomenological and the folding potentials. In [18] two families of discrete WS sets were obtained using the fitting procedure. The obtained real WS potentials have different depths and similar radii and consequently different volume integrals. At lower energies both WS sets describe the data equally well, but the deeper potentials (the WS2 set in [18]) fail to reproduce the right order of Airy minima at higher energies. This is clearly visible in the data at 200 MeV of [18] where the first Airy minimum and the rainbow angle are observed. Comparing the values of the volume integrals and the numerical values of the potentials, we may conclude that the real potential obtained in this work belongs to the same family (the WS1 set in [18]). The selection of a unique potential family results in identification of the order of Airy minima. Furthermore, it makes possible to follow the evolution of the Airy structure with energy.

B. Nearside-farside decomposition

The nearside-farside decomposition is particularly helpful in the intermediate energy range of our study. In Figs. 1 and 2, the thin-solid and dashed curves show the nearside-farside decompositions of the obtained optical model fits of the $^{16}\text{O}+^{12}\text{C}$ and the $^{18}\text{O}+^{12}\text{C}$ systems, respectively.

The angular distributions at the highest and the lowest

energy of the $^{16}\text{O}+^{12}\text{C}$ system (top and bottom panels of Fig. 1) show different patterns. The fit and calculation for the 132 MeV angular distribution display the features which are common to this and similar systems at higher energy. We can describe the angular distribution by Fraunhofer oscillations at forward angles, glory effects at backward angles, and intermediate structures, namely the deep minimum at 80° , as an Airy oscillation. The nearside-farside crossover takes place around 25° . Beyond this angle, the angular distribution is farside dominated and the structure of the distribution is refractive in its origin, i.e., it is the result of the interference between the two farside subamplitudes. By definition, the nearside and farside amplitudes are equal at 180° and their interference produces strong and rapid oscillations (glory effect) in the angular distributions as we approach the largest angles. The situation changes at lower energies. The nearside-farside crossover moves to larger angles and the Fraunhofer oscillations also extend up to large angles, they are superimposed on broad oscillations of refractive origin.

The comparison between the decompositions of the two different sets of parameters of the imaginary potential (left and right panels of Fig. 1) shows that the obtained farside components are very similar, while the nearside components exhibit quite different behavior. As already stressed, the refractive effects appear in the farside components and, omitting the different oscillatory pattern at very backward angles, the location of the Airy minima of the two different parameterizations remains the same. Such behavior clearly shows that the Airy structure is determined entirely by the real potential.

The nearside and farside components are of comparable strengths at intermediate angles for the $P(W_{\text{WS2}} + W_{\text{D}})$. The nearside recovers its strength beyond the nearside-farside crossover. For the decomposition of the calculations obtained with the $P(W_{\text{WS}})$ and shown on the right panels, the farside components behave more as was observed at higher energies, i.e., the angular distribution is farside dominated, whereas the nearside is more than two orders of magnitude smaller.

The angular distribution measured at 115.9 MeV is a typical example of the cross section in this intermediate energy range. The nearside-farside crossover takes place at 50° , 60° , and 100° for the $P(W_{\text{WS2}} + W_{\text{D}})$. The nearside and farside amplitudes become interlaced owing to their similar strengths and intersect at several points. The nearside-farside crossover takes place at 27° for the $P(W_{\text{WS}})$ and above this angle the distribution is farside dominated. Again at backward angles, the interference between the nearside (coming partly from the farside component after passing through 180° and going around) and farside components is clearly visible in the angular distribution. Looking only at the farside amplitude, two Airy minima appear in the amplitude (A_2 near 95° and A_3 near 60°) for both parameterizations. The data themselves show a wide minimumlike structure at these angles.

Owing to the stronger absorption in the $^{18}\text{O}+^{12}\text{C}$ system (see Fig. 2), even at our highest energy (120 MeV), the nearside and farside amplitudes are of similar strength throughout the whole measured angular range (top-left panel in Fig. 2) for the $P(W_{\text{WS}_2} + W_{\text{D}})$, whereas for the $P(W_{\text{WS}})$ the nearside-farside crossover is shifted toward larger angles (top-right panel in Fig. 2). The similarity of the nearside and farside strengths prolongs the appearance of the diffractivelike oscillation up to large angles. Moreover, the nearside-farside crossover moves even to larger angles as energy decreases. In the description of these data we have to keep in mind that the farside which turns over at 180° becomes the nearside, and that the structure observed at backward angles can be refractive in its origin [21,22]. In spite of this angle-extended Fraunhofer diffraction pattern the Airy minima can be discerned by considering only the farside amplitudes. In the raw data themselves the refractive effects are observed rather as irregularities in the oscillation pattern. Owing to the stronger absorption in the $^{18}\text{O}+^{12}\text{C}$ system, the nucleus-nucleus interaction transparency is reduced and the interference between the two farside subamplitudes does not dominate the angular distributions in the energy range studied. The nearside-farside decomposition with the $P(W_{\text{WS}_2} + W_{\text{D}})$ shows that the experimental distributions are nearside dominated, i.e., the diffraction is important throughout the measured angular range. We have to keep in mind that the $P(W_{\text{WS}_2} + W_{\text{D}})$ better describes the observed structure at larger angles. Nevertheless, even if the deep minima of refractive origin in the angular distribution are not observed, the description of the structure is within the refractive picture, i.e., the deep real potential is required. We want to emphasize that whenever a choice among alternative solutions of the optical potential had to be made, the main criterion was the regularity (monotonic variation) of the parameters. The regularity was based on the expectation that the potential should not change rapidly with energy and for neighboring systems. The resulting potential parameters which show such a regularity allow the connection of the observed structure in the elastic angular distributions of the $^{18}\text{O}+^{12}\text{C}$ system with the refractive effects, as observed in the neighboring and more "transparent" $^{16}\text{O}+^{16}\text{O}$ and $^{16}\text{O}+^{12}\text{C}$ systems. Since the refractive effects are not so prominent in the $^{18}\text{O}+^{12}\text{C}$ angular distributions, the optical model ambiguities remain to a certain extent.

We may conclude that in the intermediate energy range, between 5 and 10 MeV per nucleon, refractive effects are an important ingredient of the global structure of an angular distribution. The ambiguities in the determination of these refractive effects are closely related to the degree of absorption in the system. Even if the refractive effects are masked, the structure observed in the measured angular distributions can be at least partially explained as being of refractive origin. The stronger the absorption, the more masked are the refractive effects and their description becomes more complicated and less

accurate. Alternative explanations of the observed structures in angular distributions at this intermediate energy range can be helpful.

Another possibility is the decomposition into the barrier- and internal-wave (B/I) components [31,32]. The B/I decomposition makes sense if the real part of the potential is deep enough for the effective potentials to display a "potential pocket" and if the absorption is incomplete. Recently, the B/I decomposition has been applied to our data, at all energies for $^{16}\text{O}+^{16}\text{O}$ [31,32], and also at one representative energy for our nonidentical systems $^{16}\text{O}+^{12}\text{C}$ and $^{18}\text{O}+^{12}\text{C}$ [32]. Within the B/I decomposition, the Airy minima are explained as an interference of the barrier-wave and internal-wave subamplitudes. The results of the B/I decompositions for the lower and higher energy range of our $^{16}\text{O}+^{16}\text{O}$ data differ only in the relative importance of the two components. Inclusion of the surface imaginary term modifies the internal contribution only slightly, but produces the increase of the barrier cross section at large angles, which results in the increase of the yield and the presence of oscillations in the cross section. The prominence of the Airy minimum in the 132 MeV angular distribution of $^{16}\text{O}+^{12}\text{C}$ is due to similar magnitudes of the internal-wave and barrier-wave components in the angular range around 80° . Owing to the stronger absorption in the $^{18}\text{O}+^{12}\text{C}$ system, the internal-wave cross section is about three orders of magnitude lower than in the $^{16}\text{O}+^{12}\text{C}$ system, which almost completely smears out the appearance of Airy minima in the experimental angular distributions.

Very recently a semiclassical analysis of the Airy-like pattern has been presented [33]. The oscillations in the farside subamplitude are explained as a result of interference of the first and second term of a multireflection expansion of the scattering function. The physical contents and the obtained decomposition are very similar to the results of the B/I decomposition.

C. Interpretation of the results in terms of Airy minima

The rainbow and associated Airy oscillations in the scattering appear in the farside component. The Airy structure is controlled by the real potential and its appearance is often obscured by the presence of absorption. As the energy increases, the rainbow and Airy minima move forward in angle. The identification of the structures of refractive origin can be simplified by using a reduced imaginary potential. Figures 5 and 6 show the farside amplitudes with a 50% reduced imaginary strength of the $^{16}\text{O}+^{12}\text{C}$ and $^{18}\text{O}+^{12}\text{C}$ systems, respectively. The real potential is weakly dependent on energy and the smooth energy evolution of the Airy minima can be observed in the calculated distributions in Figs. 5 and 6.

Let us first discuss the results for the $^{16}\text{O}+^{12}\text{C}$ system (Fig. 5). In Refs. [18,34] the strong minimum at 80° in

the measured 132 MeV angular distribution is identified as the second Airy minimum A_2 . The minimum at 55° was identified as A_3 and that at 35° as A_4 . As already discussed, the real potentials obtained in our analysis for the $^{16}\text{O}+^{12}\text{C}$ system belong to the same family as the real potentials reported in [18]. Following the systematics of the order of Airy minima, the minima in the angular distribution at 124 MeV appearing at angles 88° , 60° , and 40° are identified as A_2 , A_3 and A_4 . At 100 MeV the A_2 minimum moves to 120° , A_3 to 80° , and A_4 to 50° . At very forward angles, around 30° , the fifth Airy minimum can also be discerned in the farside component at 100 MeV. Of course, it is not easy to see the remnants of all these minima in the actual data, especially for the higher-order minima appearing at more forward angles where strong Fraunhofer oscillations are dominant.

No detailed elastic angular distributions at the $^{18}\text{O}+^{12}\text{C}$ system for energies higher than those in the present study (where one expects a more favorable situation for the identification of the Airy minima and their order) have been reported so far. In the identification of the order of Airy minima, we assume a similar behavior in the $^{18}\text{O}+^{12}\text{C}$ and $^{16}\text{O}+^{12}\text{C}$ systems. Therefore, it is likely that the A_2 and A_3 minima appear in $^{18}\text{O}+^{12}\text{C}$ at energies around 100 MeV as well. According to this assumption, the minimum around 105° in the 120 MeV angular distribution is labeled as A_2 , and the minima at 75° , 50° , and at the very forward angle of 30° as A_3 , A_4 , and A_5 (see Fig. 6). The minima move to larger angles at lower energies and at 100 MeV the A_3 moves to 105° , A_4 to 72° , and A_5 to 45° . At 85 MeV, even the A_6 can be discerned at a very forward angle.

The positions of the Airy minima as a function of center-of-mass energy for both systems studied are shown in Figs. 7 and 8. A very regular parabolic behavior is observed.

The angles at which the minima take place in the farside amplitudes do not depend on the imaginary potential strength and no important angular shift is observed if the absorption is switched on. The depth of the minima in the farside changes with absorption. The absorption dictates which minimum will be dominant in the farside amplitude. The stronger the absorption, the deeper the minima will be at larger angles and conversely at smaller angles. It has to be noted that the interference between the volume and surface components introduces some additional small oscillations around the Airy minima. This speaks in favor of the conclusion that the volume and surface absorptive components play different roles.

D. Potentials, volume integrals, and global systematics

In this section we present all optical potentials obtained for the four systems considered in our study: $^{16}\text{O}+^{16}\text{O}$ [19–21], $^{16}\text{O}+^{12}\text{C}$ [22–24], $^{18}\text{O}+^{12}\text{C}$ [23,24],

and $^{12}\text{C}+^{12}\text{C}$ [7,24,35]. Figure 9 shows the energy and system variations of the obtained potentials (real and imaginary parts) at representative energies of the energy range studied.

In all systems, a deep real part is required for a good description of the elastic angular distributions. The observed structure in the distributions is explained through refractive effects. The imaginary part changes from system to system. While the inclusion of the surface term was needed only for the lower energy range in $^{16}\text{O}+^{16}\text{O}$, the $^{16}\text{O}+^{12}\text{C}$ system required a surface term for all energies, and without it the structure at larger angles cannot be well described. The surface term becomes even more important in the obtained imaginary potential of the $^{18}\text{O}+^{12}\text{C}$ system. When the surface term is needed, the absorptive potential has a characteristic shape: a volume term which tends to have a small diffuseness plus a Gaussian-like surface peak.

The most typical examples of such a shape are the optical potentials for $^{16}\text{O}+^{16}\text{O}$ at 75 MeV, for $^{16}\text{O}+^{12}\text{C}$ at 124 MeV, and for $^{18}\text{O}+^{12}\text{C}$ at all energies studied. Within a simple interpretation, we can associate the volume term with the absorption due to fusion and related processes, and the surface term with more direct reactions. These different shapes of the absorptive potential can be explained as a consequence of the evolution of the reaction mechanisms which change from the fusion type to a more direct type of reaction. This enhancement of the surface integral is a signature of a larger number of open direct reaction channels and is in agreement with the number of open channel calculations [1]. Complementary studies of the distribution of the incident flux into the different available exit binary channels, as well as of the underlying reaction mechanisms are actually underway for the $^{16}\text{O}+^{12}\text{C}$ and $^{18}\text{O}+^{12}\text{C}$ reactions.

Table III lists the real and imaginary volume integrals of the potentials obtained for the oxygen+carbon systems studied and for the two adopted sets of parameters. The real and imaginary volume integrals display a smooth behavior with energy. The real volume integral generally decreases with energy, while the imaginary volume integral increases. Such behavior is in agreement with the dispersion relation predictions. Although the shapes of the imaginary potential are radically different for the two sets of parameters, the full imaginary volume integrals (columns 5 and 7 of Table III) are about the same.

In the review article of Brandan and Satchler [4], the values of the real and imaginary volume integrals as a function of projectile energy per nucleon for the potentials that fit the $^{12}\text{C}+^{12}\text{C}$, $^{16}\text{O}+^{16}\text{O}$, and $^{16}\text{O}+^{12}\text{C}$ data have been extracted (see Fig. 6.7 of [4]). It is shown that the different real potentials all have similar volume integrals and that the imaginary volume integrals show a smooth behavior as a function of energy in spite of various parameterizations adopted for the imaginary potentials. It is quite remarkable to notice that the volume integrals reported in our work closely follow the global

systematics evidenced in [4].

V. CONCLUSION

In this paper we have presented the elastic scattering data of the $^{16}\text{O}+^{12}\text{C}$ and $^{18}\text{O}+^{12}\text{C}$ reactions, together with the optical model analysis. We have used the nearside-farside decomposition technique to interpret the complicated features of the angular distributions. The elastic angular distributions show not only the usual Fraunhofer diffraction pattern, but also, at larger angles, refractive effects in the form of nuclear rainbow Airy structures. The main features of the measurements are very well described by the optical model fits. A deep real part is required for the description of refractive effects. The imaginary potential is weakly absorptive and reflects the presence of incomplete absorption. The two studied systems, $^{16}\text{O}+^{12}\text{C}$ and $^{18}\text{O}+^{12}\text{C}$, have different shapes of the imaginary potentials and different values of the volume imaginary integrals. The volume imaginary integral increases for the $^{18}\text{O}+^{12}\text{C}$ system, mostly in the imaginary surface part. The enhancement of the surface integral is a signature of a larger number of open direct reaction channels. This conclusion is supported by the study of the inelastic and transfer channels, as well as by the number of open channel calculations.

The inclusion of the surface imaginary term provides the needed increase of the yield at large angles, but also defines a characteristic shape of the imaginary potential. When the surface term is required by the data, the imaginary volume term tends to have a small diffusseness and a smaller radius than the surface imaginary term. One can imagine that the reflection from a potential with such a profile may produce additional interferences resulting in more structured angular distributions at larger angles. As has been mentioned, the effects of elastic transfer could also cause an increase of the yield at the largest angles and additional structure in the angular distributions. The specific imaginary potential obtained here can be understood through coupling effects which should have an impact on the elastic angular distribution. An additional analysis like the explicit inclusion of elastic transfer could provide a better understanding of the origin of the large angle structures, but it is unlikely that this would appreciably change the results for the real part of the potential. Therefore, the most important conclusion about the depth of the real potential, the potential which describes the refractive effects and defines the position of the Airy minima, will remain unchanged.

The appearance of refractive structures permits an unambiguous determination of the optical potential. Within this analysis we do not claim that the obtained potentials are unique, energy by energy. What we believe as unique is the regularity and systematics of the potentials as a function of energy and also of the target and projectile matter distribution. The obtained potentials

for the light heavy-ion systems studied have a deep real part and a weakly absorbing imaginary part. In spite of the differences in the shape of the imaginary potentials for the $^{12}\text{C}+^{12}\text{C}$, $^{16}\text{O}+^{16}\text{O}$, $^{16}\text{O}+^{12}\text{C}$, and $^{18}\text{O}+^{12}\text{C}$ systems (see Fig. 9) the volume imaginary integrals agree with the global systematics (evidenced in [4]). The systematics is based on the refractive nature of light heavy-ion collisions and is in agreement with the dispersion relation predictions. The obtained volume integrals, both real and imaginary, agree with potentials which fit the higher and lower energy data.

We may thus conclude that in the intermediate energy region, between 5 and 10 MeV per nucleon, the refractive effects, although masked partially by diffraction, are still strong enough to permit a simple mean-field optical-model explanation of the main structures of the elastic scattering cross sections.

VI. ACKNOWLEDGMENTS

We are indebted to A.A. Ogloblin and his group for making their experimental angular distributions available to us. We would also like to thank Dao T. Khoa for providing us with his nearside/farside decomposition codes as well as with a UNIX adapted version of the code PTOLEMY.

TABLE I. Phenomenological potentials, the real part is a WS2 term and the imaginary part is a sum of the WS2 (volume) plus WSD (surface) term. V and the subscript V stand for the real term, W and the subscript W for the volume imaginary term and the subscript D for the surface imaginary term. The a_W could be fixed arbitrarily at some small value, such as 0.1 fm, without much influence on the fits, but we prefer to report the values resulting from the automatic search.

$^{16}\text{O}+^{12}\text{C}$ $R_V=4$ fm, $a_V=1.4$ fm								
E_{lab}	$E_{\text{c.m.}}$	V	W	R_W	a_W	W_D	R_D	a_D
[MeV]	[MeV]	[MeV]	[MeV]	[fm]	[fm]	[MeV]	[fm]	[fm]
132	56.6	292	24.6	3.190	0.420	11.3	4.880	0.640
124	53.2	296	14.7	4.399	0.170	9.3	5.985	0.453
115.9	49.7	288	16.0	4.464	0.111	7.1	6.097	0.460
100	42.9	288	10.5	5.466	0.190	3.8	6.640	0.440
94.8	40.6	285	11.4	5.351	0.156	3.6	6.708	0.360
80.0	34.3	278	13.9	5.256	0.170	2.5	6.849	0.438
$^{18}\text{O}+^{12}\text{C}$ $R_V=4.08$ fm, $a_V=1.38$ fm								
E_{lab}	$E_{\text{c.m.}}$	V	W	R_W	a_W	W_D	R_D	a_D
[MeV]	[MeV]	[MeV]	[MeV]	[fm]	[fm]	[MeV]	[fm]	[fm]
120	48	298	22.6	3.910	0.059	11.6	5.750	0.528
100	40	310	22.0	4.100	0.047	11.0	5.730	0.540
85	34	326	20.7	4.157	0.055	10.5	5.743	0.551

TABLE II. Phenomenological potentials, the real part is a WS2 term and the imaginary part is a WS1 term (pure volume).

$^{16}\text{O}+^{12}\text{C}$ $R_V=4$ fm, $a_V=1.4$ fm					
E_{lab}	$E_{\text{c.m.}}$	V	W	R_W	a_W
[MeV]	[MeV]	[MeV]	[MeV]	[fm]	[fm]
132	56.6	293	13.4	5.900	0.603
124	53.2	290	14.1	5.712	0.636
115.9	49.7	290	13.0	5.878	0.522
100	42.9	297	10.4	6.079	0.523
94.8	40.6	297	8.8	6.672	0.317
80.0	34.3	297	9.0	6.557	0.322
$^{18}\text{O}+^{12}\text{C}$ $R_V=4.08$ fm, $a_V=1.38$ fm					
E_{lab}	$E_{\text{c.m.}}$	V	W	R_W	a_W
[MeV]	[MeV]	[MeV]	[MeV]	[fm]	[fm]
120	48	293	13.4	6.443	0.523
100	40	305	13.9	6.270	0.615
85	34	324	18.3	5.930	0.562

TABLE III. Volume integrals for the potentials obtained in $^{16}\text{O}+^{12}\text{C}$ and $^{18}\text{O}+^{12}\text{C}$. $W_{\text{WS2}} + W_D$ stands for the parameters listed in Table I and W_{WS} for the parameters in Table II.

$^{16}\text{O}+^{12}\text{C}$						
Energy	$W_{\text{WS2}} + W_D$				W_{WS}	
	J_V	J_W	J_{WD}	$J_W + J_{WD}$	J_V	J_W
132	312	13	48	61	313	66
124	316	24	40	64	309	64
115.9	308	29	32	61	310	62
100	308	34	20	54	317	55
94.8	304	35	16	51	317	58
80	297	40	14	54	317	56
$^{18}\text{O}+^{12}\text{C}$						
Energy	$W_{\text{WS2}} + W_D$				W_{WS}	
	J_V	J_W	J_{WD}	$J_W + J_{WD}$	J_V	J_W
120	296	25	48	73	292	74
100	309	28	47	75	304	73
85	325	28	46	74	323	81

FIG. 1. Elastic scattering data shown as the ratio to the Rutherford cross sections and optical model calculations (thick-solid curves) with phenomenological potentials (left panels with parameters from Table I, and right panels from Table II) of the $^{16}\text{O}+^{12}\text{C}$ at 132, 124, 115.9, and 100 MeV (from top to bottom, left and right, respectively). The near-side (thin-solid curve) and farside (dashed curve) subamplitudes for different potentials are plotted.

FIG. 2. Same caption as for Fig. 1 but for the $^{18}\text{O}+^{12}\text{C}$ elastic scattering at 120, 100, and 85 MeV.

FIG. 3. Measured elastic angular distributions displayed as ratio to the Rutherford scattering of the $^{16}\text{O}+^{12}\text{C}$ (stars, panel *a*) and $^{18}\text{O}+^{12}\text{C}$ scattering (dots, panels *b* and *c*) at an incident energy of 100 MeV. The solid curve (parameters from Table I) and dashed curve (parameters from Table II) of panels *a* and *c* represent optical-potential fits. The same fits are presented in Fig. 1 (bottom panel) and Fig. 2 (middle panel). The solid [$P(W_{\text{WS}} + W_{\text{D}})$] and dashed curves [$P(W_{\text{WS}})$] of panel *b* represent optical-potential calculations using the parameters obtained in the $^{16}\text{O}+^{12}\text{C}$ fit but changing the projectile mass.

FIG. 4. The real and imaginary potentials at 100 MeV of the $^{16}\text{O}+^{12}\text{C}$ (left-top panel, and solid curves in bottom panels) and $^{18}\text{O}+^{12}\text{C}$ (right-top panel and dashed curves in bottom panels) for the two sets of parameters listed in Tables I and II.

FIG. 5. The calculated farside amplitudes for all measured energies of the $^{16}\text{O}+^{12}\text{C}$ system using the parameters from Table I. The imaginary strength has been reduced by 50% to emphasize the refractive effects. Curves at different energies have been shifted by a factor of 100 for clarity.

FIG. 6. Same caption as for Fig. 5 but for the $^{18}\text{O}+^{12}\text{C}$ system.

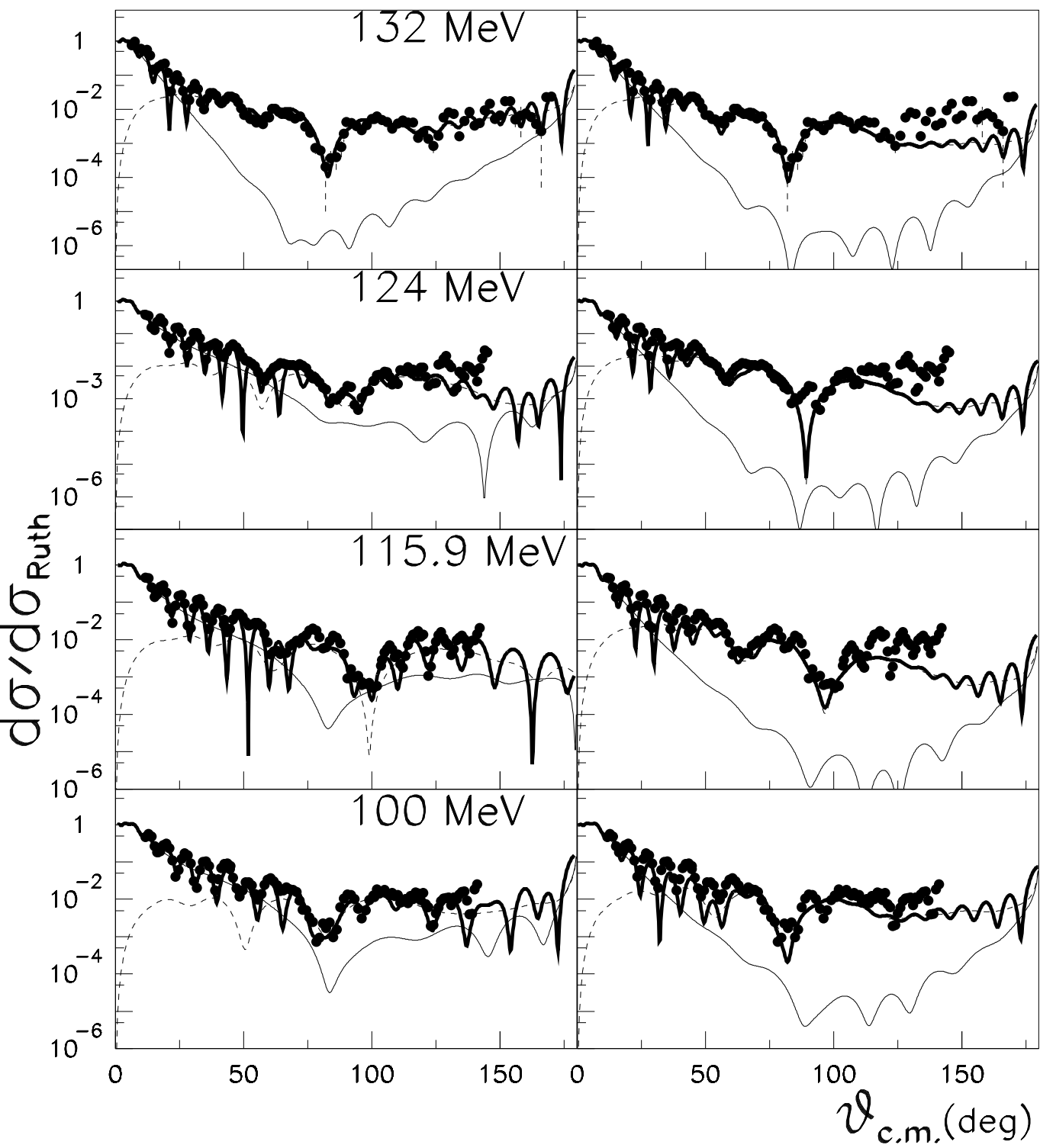
FIG. 7. The position of Airy minima ($\theta_{\text{c.m.}}$ versus $E_{\text{c.m.}}$) of the $^{16}\text{O}+^{12}\text{C}$ system. The solid curves are results of the χ^2 fit to the data using the second-order polynomial as the fit function.

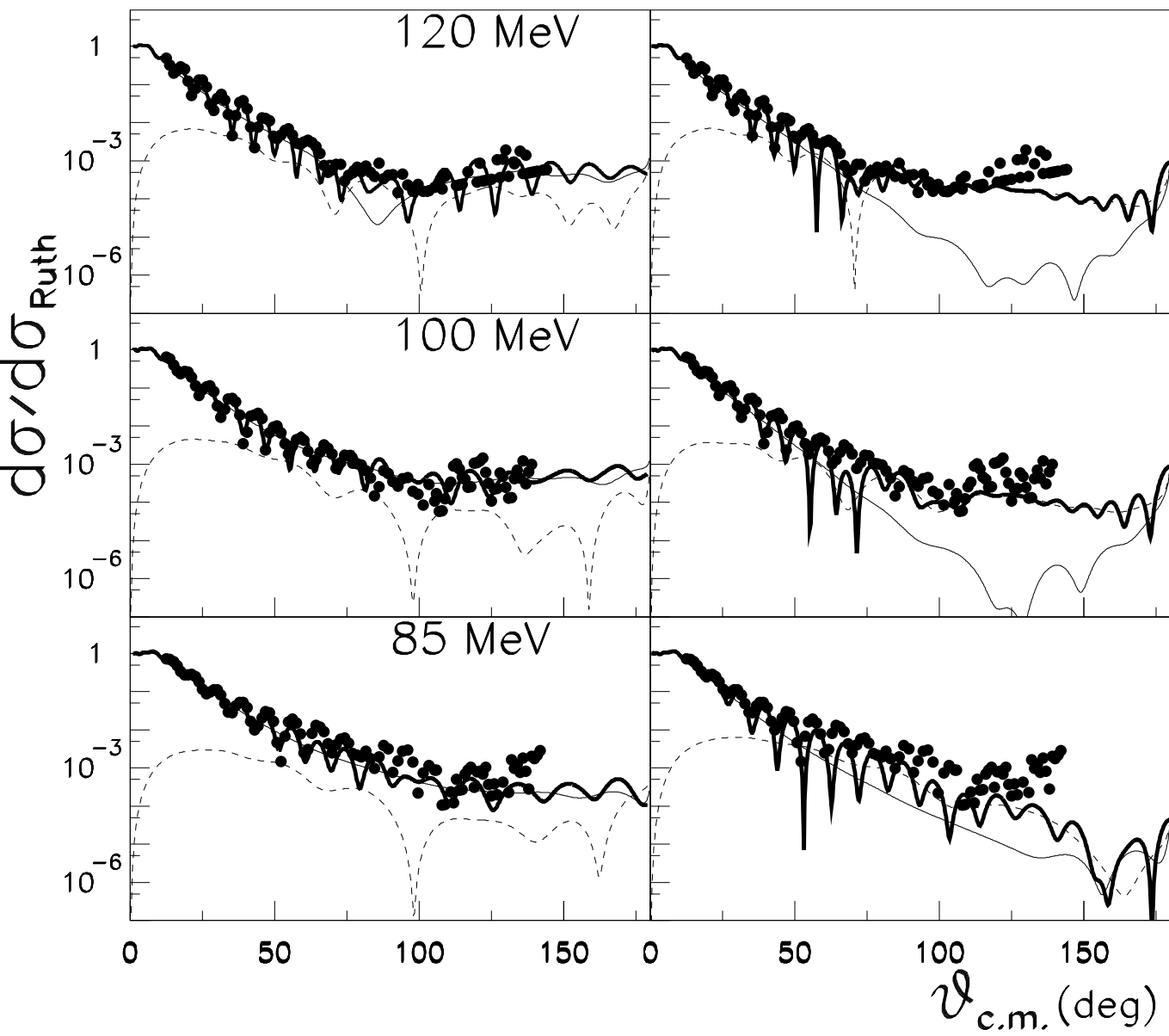
FIG. 8. Same caption as for Fig. 7 but for the $^{18}\text{O}+^{12}\text{C}$ system.

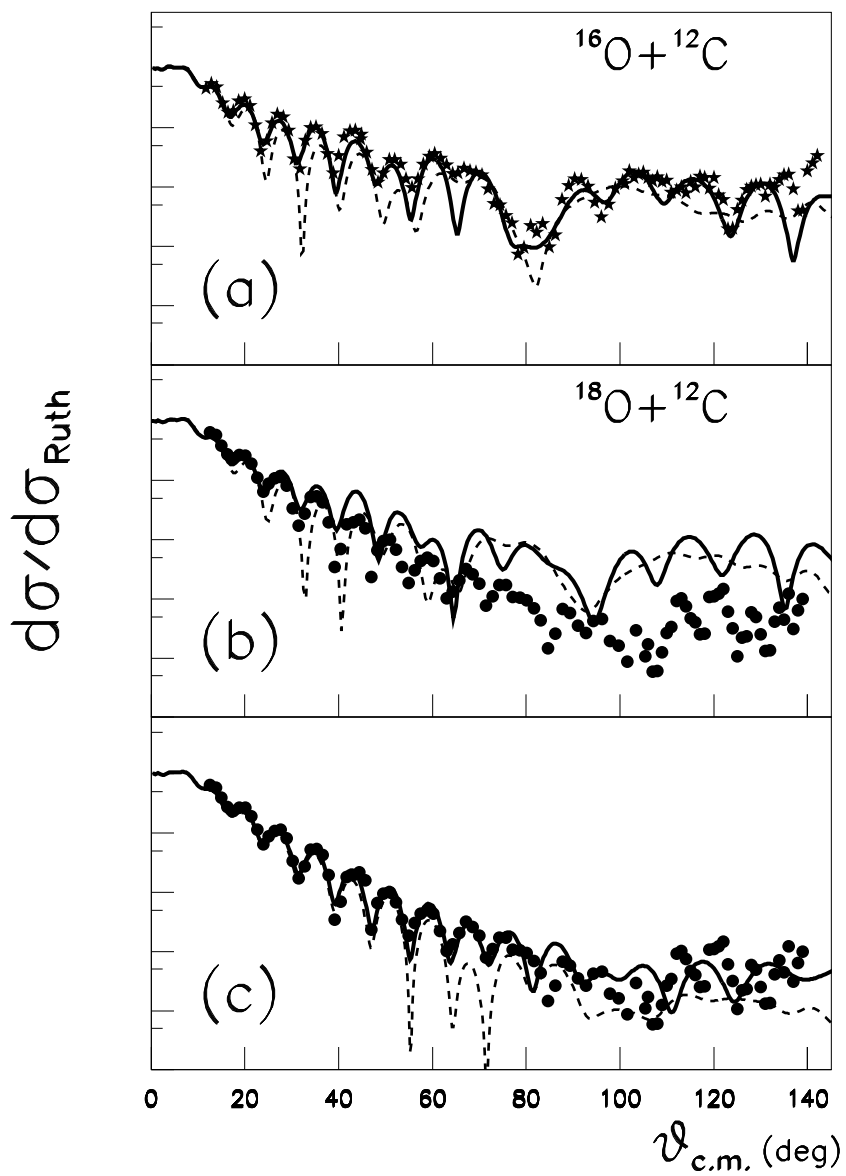
FIG. 9. Real and imaginary parts of the phenomenological optical potentials obtained for the $^{12}\text{C}+^{12}\text{C}$, $^{16}\text{O}+^{16}\text{O}$, $^{16}\text{O}+^{12}\text{C}$, and $^{18}\text{O}+^{12}\text{C}$ systems at three different energies.

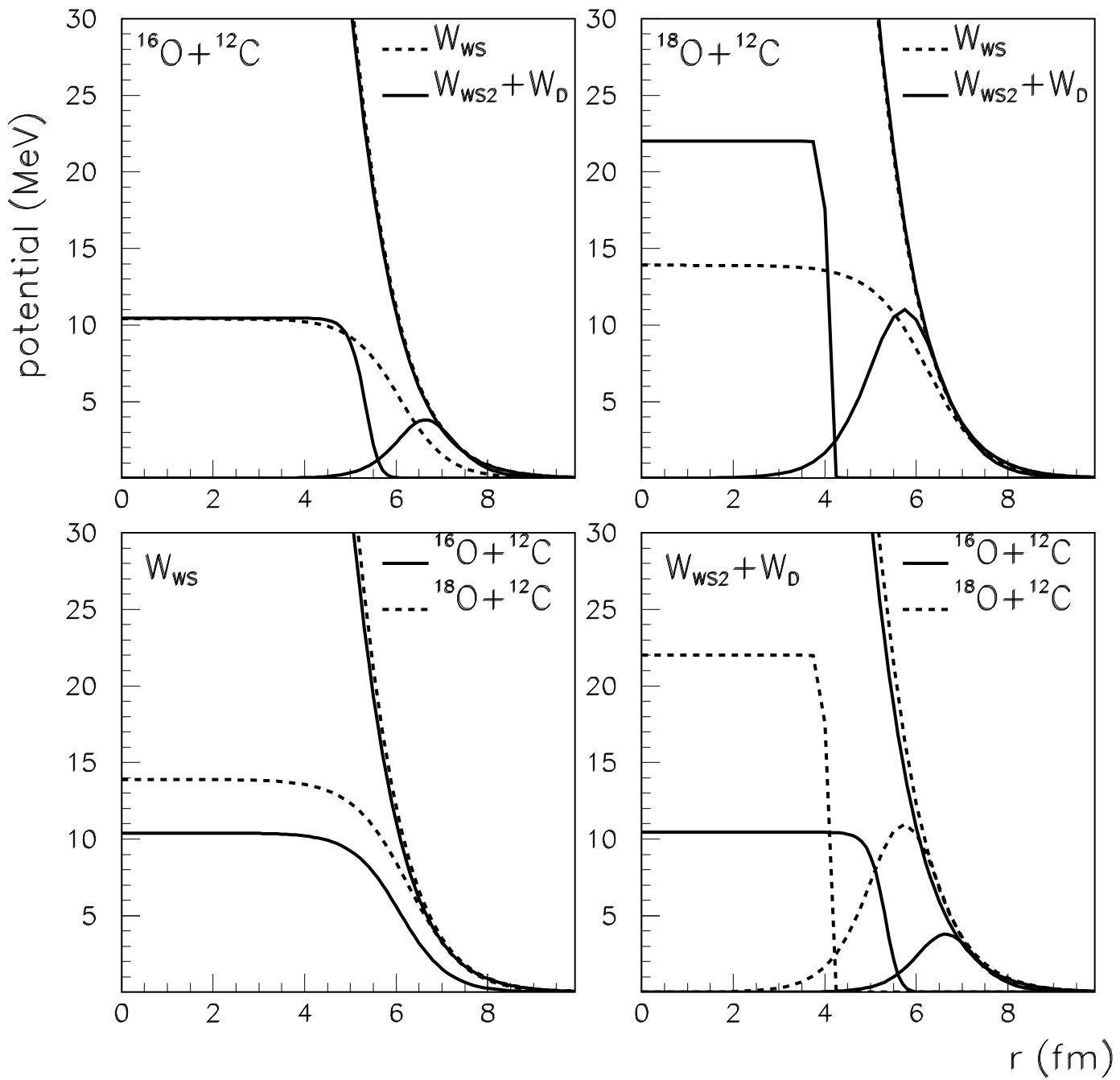
-
- [1] F. Haas, and Y. Abe, *Phys. Rev. Lett.* **46**, 1667 (1981).
 - [2] R.R. Betts, and A.H. Wuosmaa, *Rep. Prog. Phys.* **60**, 819 (1997).
 - [3] R.R. Betts, *Proc. of the 7th Int. Conf. on Clustering Aspects of Nuclear Structure and Dynamics*, Rab, Croatia, 1999, eds. M. Korolija, Z. Basrak, and R. Čaplar, World Scientific, p. 109 and references therein.
 - [4] M.E. Brandan, and G.R. Satchler, *Phys. Rep.* **285**, 143 (1997) and references therein.
 - [5] R.G. Stokstad, R.M. Wieland, G.R. Satchler, C.B. Fulmer, D.C. Hensley, S. Raman, L.D. Rickertsen, A.H. Snell, and P.H. Stelson, *Phys. Rev. C* **20**, 655 (1979).
 - [6] M.E. Brandan, M. Rodríguez-Villafuerte, and A. Ayala, *Phys. Rev. C* **41**, 1520 (1990).
 - [7] A. Morsad, F. Haas, C. Beck, and R.M. Freeman, *Z. Phys. A* **338**, 61 (1991).
 - [8] Dao T. Khoa, W. von Oertzen, H.G. Bohlen, and F. Nuoffer, *Nucl. Phys.* **A672**, 387 (2000).
 - [9] E. Stiliaris, H.G. Bohlen, P. Fröbrich, B. Gebauer, D. Kolbert, W. von Oertzen, M. Wilpert, and Th. Wilpert, *Phys. Lett. B* **223**, 91 (1989).
 - [10] Y. Kondō, Y. Sugiyama, Y. Tomita, Y. Yamanouchi, H. Ikezoe, K. Ideno, S. Hamada, T. Sugimitsu, M. Hijiya, and H. Fujita, *Phys. Lett. B* **365**, 17 (1996).
 - [11] A.A. Ogloblin, Dao T. Khoa, Y. Kondō, Yu.A. Glukhov, A.S. Dem'yanova, M.V. Rozhkov, G.R. Satchler, and S.A. Goncharov, *Phys. Rev. C* **57**, 1797 (1998).
 - [12] M.E. Brandan, and A. Menchaca-Rocha, *Phys. Rev. C* **23**, 1272 (1981).
 - [13] M.E. Brandan, A. Menchaca-Rocha, M. Buenerd, J. Chauvin, P. DeSaintignon, G. Duhamel, D. Lebrun, P. Martin, G. Perrin, and J.Y. Hostachy, *Phys. Rev. C* **34**, 1484 (1986).
 - [14] P. Roussel, N. Alamanos, F. Auger, J. Barrette, B. Berthier, B. Fernandez, L. Papineau, H. Doubre, and W. Mittig, *Phys. Rev. Lett.* **54**, 1779 (1985).
 - [15] U.C. Voos, W. von Oertzen, and R. Bock, *Nucl. Phys.* **A135**, 207 (1969).

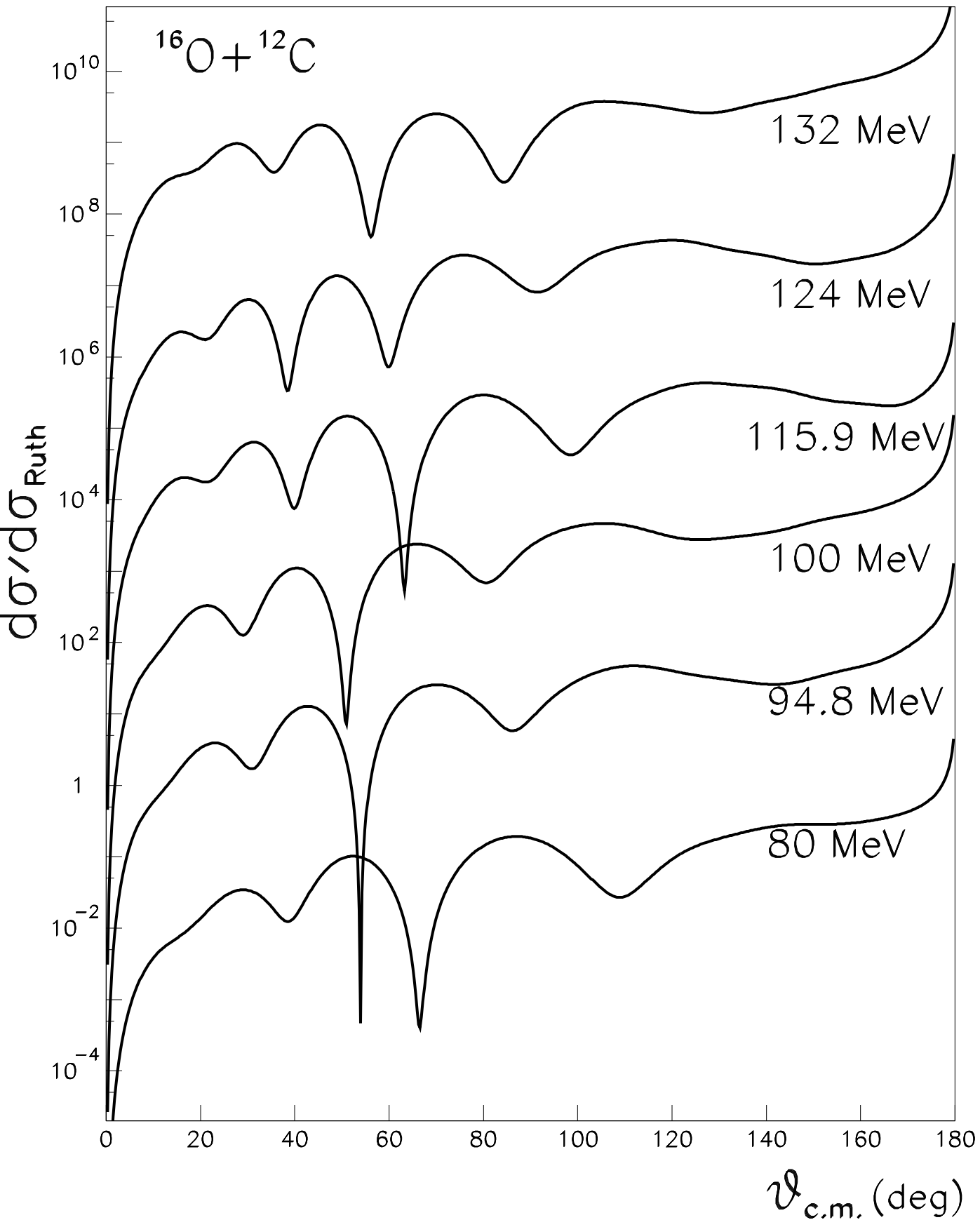
- [16] H.H. Gutbrod, R. Bock, W. von Oertzen, and U.C. Schlotthauer-Voos, *Z. Phys.* **262**, 377 (1973).
- [17] C. Gao, and Y. Kondō, *Phys. Lett. B* **408**, 7 (1997).
- [18] A.A. Ogloblin, Yu. A. Glukhov, W.H. Trzaska, A.S. Dem'yanova, S.A. Goncharov, R. Julin, S.V. Klebnikov, M. Mutterer, M.V. Rozhkov, V.P. Rudakov, G.P. Tiorin, Dao T. Khoa, and G.R. Satchler, *Phys. Rev. C* **62**, 044601 (2000).
- [19] M.P. Nicoli, F. Haas, R.M. Freeman, S. Szilner, Z. Basrak, A. Morsad, N. Aissaoui, C. Beck, A. Elanique, and R. Nouicer, *Nucl. Phys.* **A654**, 882c (1999).
- [20] M.P. Nicoli, F. Haas, R.M. Freeman, N. Aissaoui, C. Beck, A. Elanique, R. Nouicer, A. Morsad, S. Szilner, and Z. Basrak, *Proc. of the 36th International Winter Meeting on Nuclear Physics*, Bormio, Italy, 1998, p. 529
- [21] M.P. Nicoli, F. Haas, R.M. Freeman, N. Aissaoui, C. Beck, A. Elanique, R. Nouicer, A. Morsad, S. Szilner, Z. Basrak, M.E. Brandan, and G.R. Satchler, *Phys. Rev. C* **60**, 064608 (1999).
- [22] M.P. Nicoli, F. Haas, R.M. Freeman, S. Szilner, Z. Basrak, A. Morsad, G.R. Satchler, and M.E. Brandan, *Phys. Rev. C* **61**, 034609 (2000).
- [23] S. Szilner, M.P. Nicoli, Z. Basrak, R.M. Freeman, F. Haas, and A. Morsad, *Proc. of the 7th Int. Conf. on Clustering Aspects of Nuclear Structure and Dynamics*, Rab, Croatia, 1999, eds. M. Korolija, Z. Basrak and R. Čapljar, World Scientific, p. 180.
- [24] S. Szilner, M.P. Nicoli, Z. Basrak, R.M. Freeman, F. Haas, A. Morsad, M.E. Brandan, and G.R. Satchler, *Proc. of the 38th International Winter Meeting on Nuclear Physics*, Bormio, Italy, 2000, p. 510.
- [25] M.P. Nicoli, *Thèse de Doctorat de l'Université Louis Pasteur*, Strasbourg, 1998, IReS 98-16 Report.
- [26] S. Szilner, *Ph.D. thesis*, Université Louis Pasteur, Strasbourg and University of Zagreb, 2001, IReS 01-03 Report.
- [27] R.M. Freeman, Z. Basrak, F. Haas, A. Hachem, G.A. Monnehan, and M. Youlal, *Z. Physik A* **341**, 175 (1992).
- [28] Dao T. Khoa, G.R. Satchler, and W. von Oertzen, *Phys. Rev. C* **56**, 954 (1997).
- [29] M.H. Macfarlane, and S.C. Pieper, Argonne National Laboratory Report, ANL-76-11 (1978)
- [30] R.C. Fuller, *Phys. Rev. C* **12**, 1561 (1975).
- [31] F. Michel, F. Brau, G. Reidemeister, and S. Ohkubo, *Phys. Rev. Lett.* **85**, 1823 (2000).
- [32] F. Michel, G. Reidemeister, and S. Ohkubo, *Phys. Rev. C* **63**, 034620 (2001).
- [33] R. Anni, *Phys. Rev. C* **63**, 031601 (2001).
- [34] G.R. Satchler *et al.* (unpublished).
- [35] S. Szilner, Z. Basrak, R.M. Freeman, F. Haas, A. Morsad, M.P. Nicoli, and C. Beck, *J.Phys. G: Nucl. Part. Phys.* **25**, 1927 (1999).

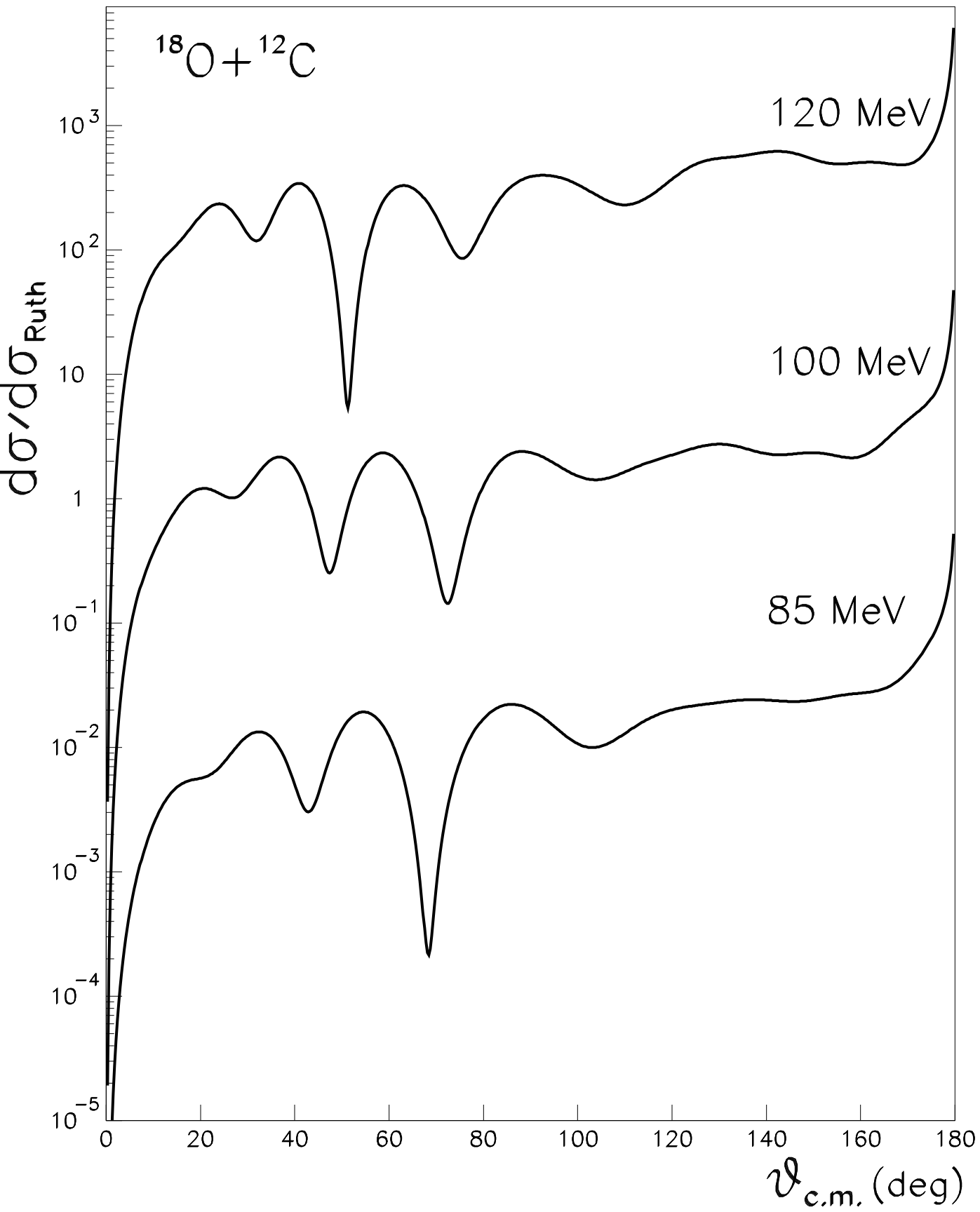


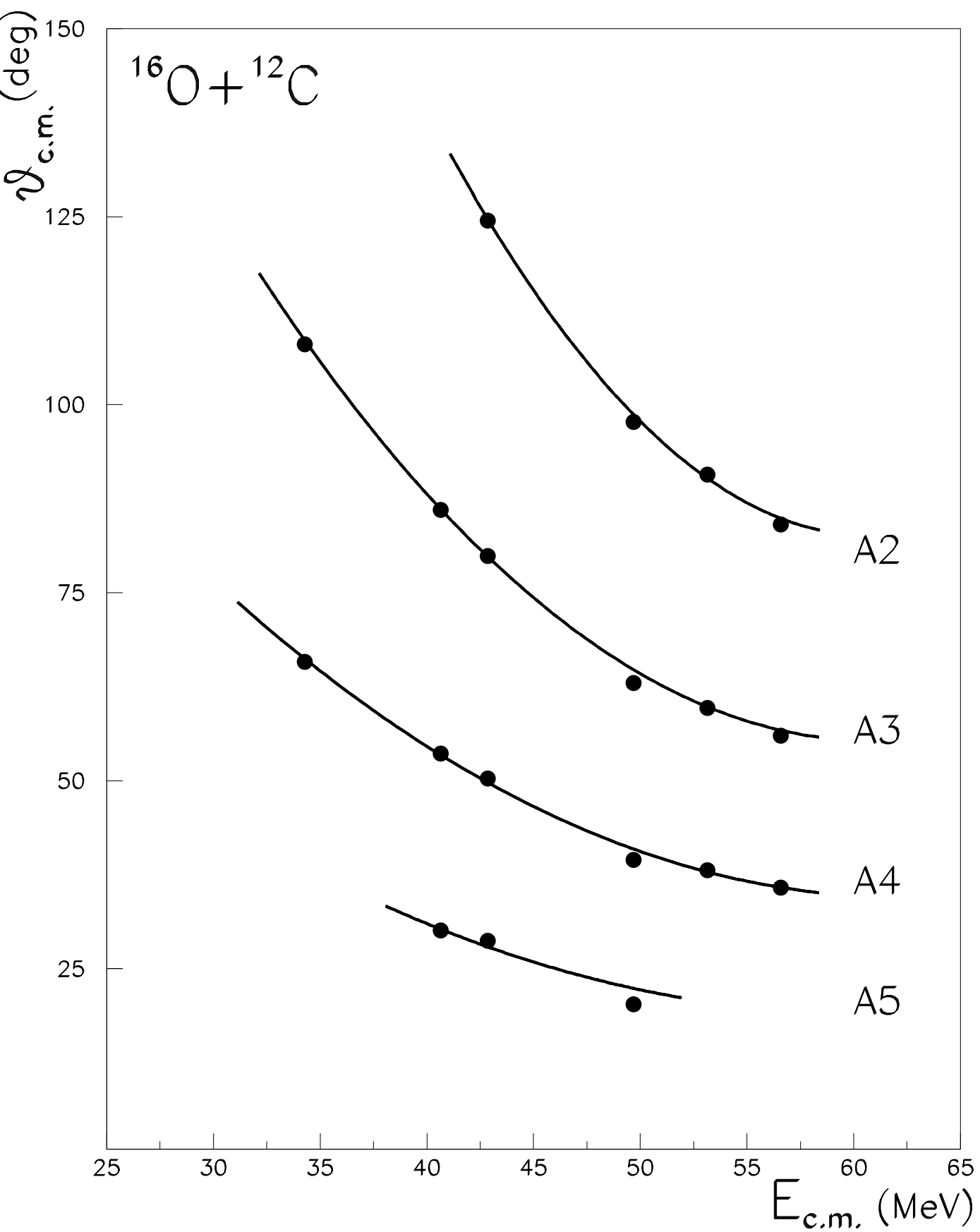


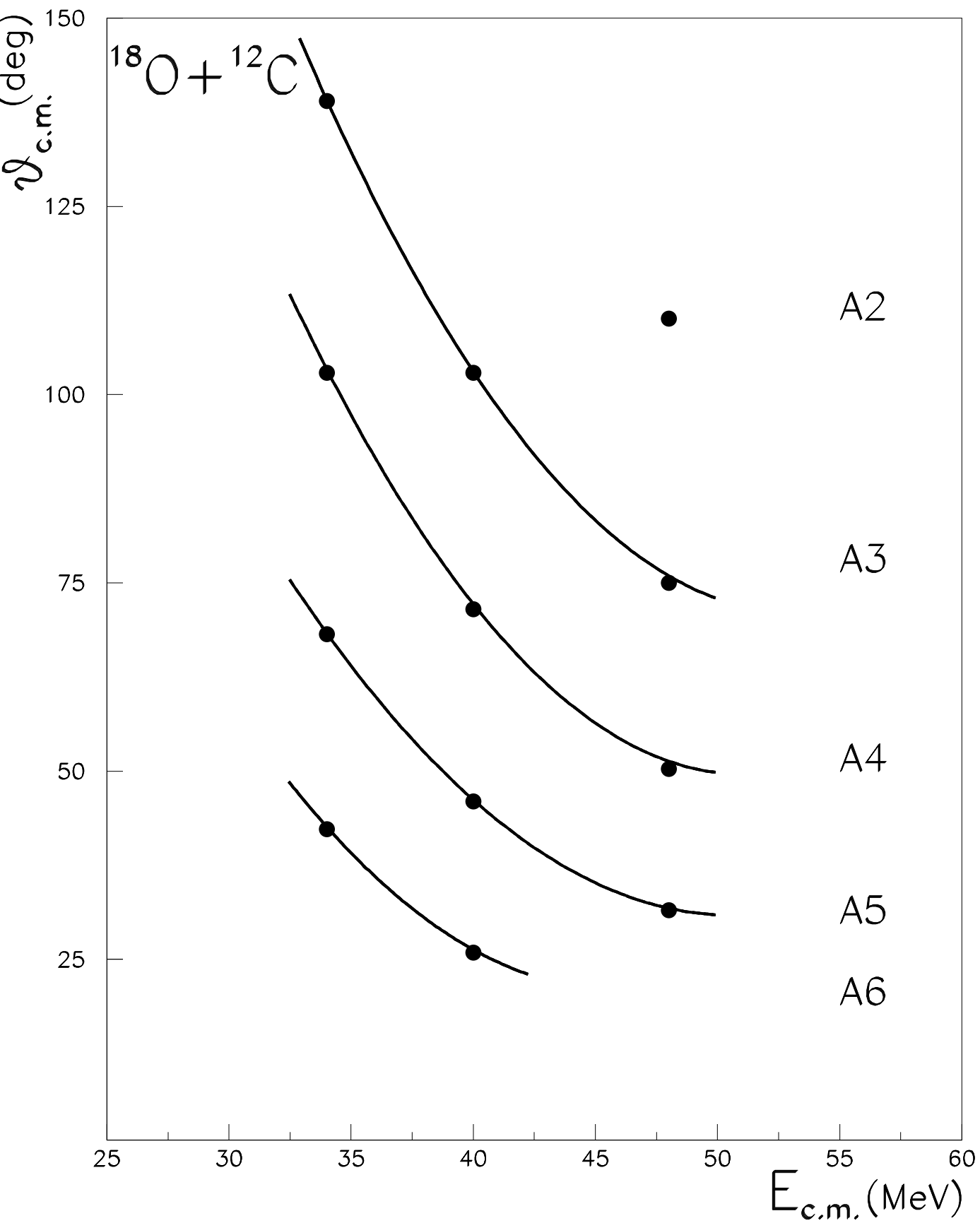




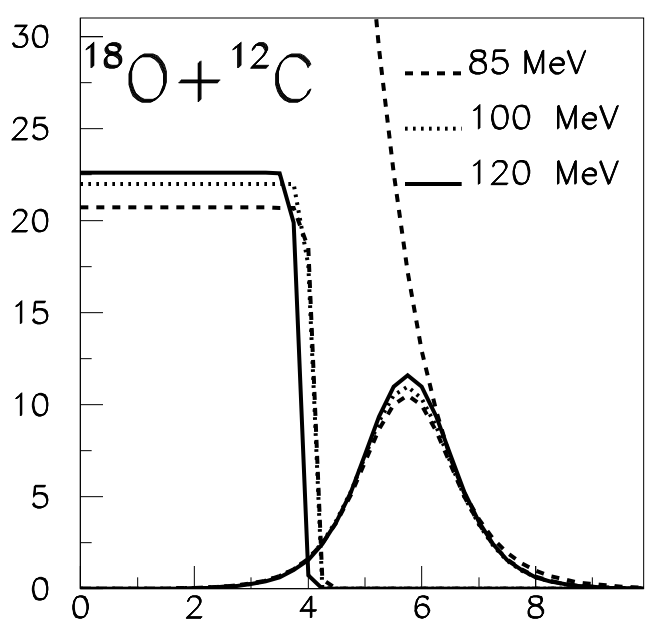
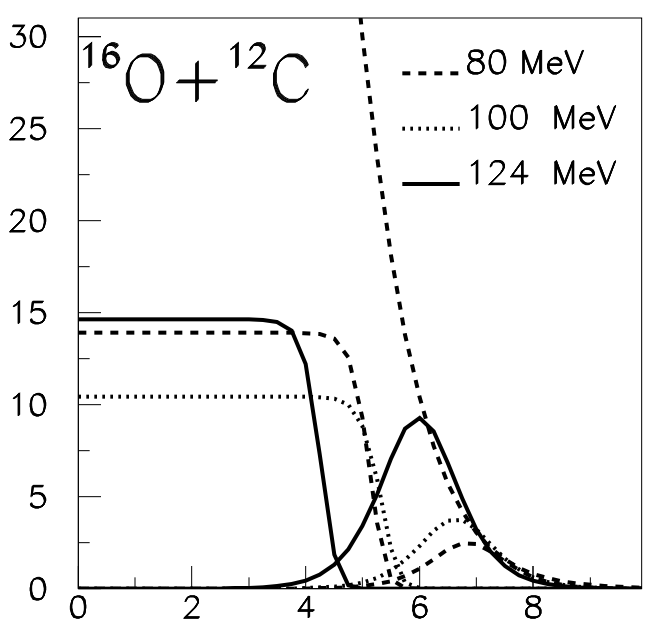
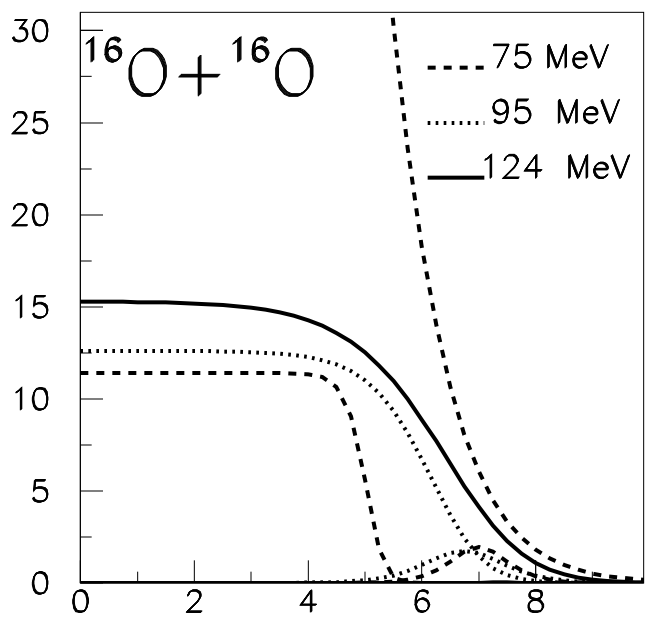
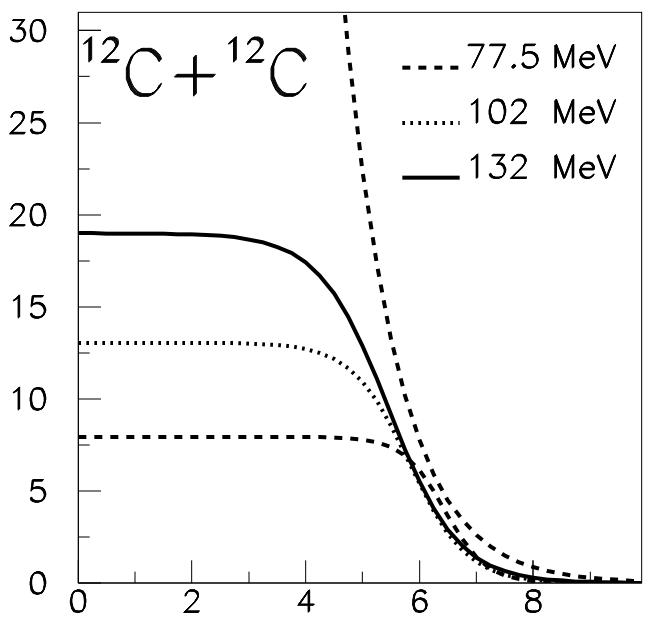








potential (MeV)



r (fm)